
This is an electronic reprint of the original article.
This reprint may differ from the original in pagination and typographic detail.

Puttonen, Tuomas; Salmi, Mika; Partanen, Jouni

Mechanical properties and fracture characterization of additive manufacturing polyamide 12 after accelerated weathering

Published in:
Polymer Testing

DOI:
[10.1016/j.polymertesting.2021.107376](https://doi.org/10.1016/j.polymertesting.2021.107376)

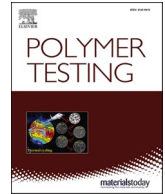
Published: 01/12/2021

Document Version
Publisher's PDF, also known as Version of record

Published under the following license:
CC BY

Please cite the original version:
Puttonen, T., Salmi, M., & Partanen, J. (2021). Mechanical properties and fracture characterization of additive manufacturing polyamide 12 after accelerated weathering. *Polymer Testing*, 104, Article 107376. <https://doi.org/10.1016/j.polymertesting.2021.107376>

This material is protected by copyright and other intellectual property rights, and duplication or sale of all or part of any of the repository collections is not permitted, except that material may be duplicated by you for your research use or educational purposes in electronic or print form. You must obtain permission for any other use. Electronic or print copies may not be offered, whether for sale or otherwise to anyone who is not an authorised user.



Mechanical properties and fracture characterization of additive manufacturing polyamide 12 after accelerated weathering

Tuomas Puttonen^{*}, Mika Salmi, Jouni Partanen

Aalto University School of Engineering, Department of Mechanical Engineering Otakaari 4, 02150, Espoo, Finland

ARTICLE INFO

Keywords:

Additive manufacturing
Powder bed fusion
Accelerated weathering
Polymer degradation
Mechanical properties
Fracture characterization

ABSTRACT

The additive manufacturing (AM) methods, selective laser sintering (SLS) and multi jet fusion (MJF), are increasingly used for end-use polymer parts. Chemical reactions caused by ionizing radiation and catalyzed by oxygen, moisture, and heat are known to degrade the polymer structure, result in visual defects, and loss of mechanical properties. However, the effects of the AM layer-wise manufacturing process on polymer degradation are not widely studied. Yet, they may have implications on the mechanical properties and fracture mechanisms of the components.

This paper presents an open access data repository of mechanical properties after weathering for AM plastics, conventionally manufactured plastics, and for two clear protective coatings. All materials were exposed to a 1500-h accelerated weathering cycle (ISO-4982-3) followed by tensile testing (ISO-527). Special attention was given to polyamide 12 (PA12) produced via powder bed fusion AM in two build orientations. The fracture surfaces of PA12 and glass-filled PA12 were further studied with scanning electron microscopy. The AM materials were PA12, glass-filled PA12, and carbon reinforced PA12. Traditionally manufactured materials included glass-filled and molybdenum disulfide-filled PA66, PMMA, ABS, PC, and cast PA12.

No clear differences were found between the AM build orientations in fracture mechanisms or weathering performance. AM and cast PA12 were strongly affected by accelerated weathering. Carbon reinforced PA12 with a UV varnish experienced the least changes. Weathering resistance was increased with protective coatings. However, an increase in the deviation of mechanical properties with the coatings was observed. The contrary results in ductility for the glass-filled and molybdenum disulfide-filled PA66 after weathering would merit further studies.

1. Introduction

Plastics are a material class developed and studied extensively from the early 20th century and have been mass-produced now for almost a hundred years [1]. Their light weight, adaptable mechanical properties, and easy manufacturability make them suitable for the manufacture of products ranging from disposable packaging to high-end engineering applications. In comparison to the history of plastics, additive manufacturing (AM) is a very young manufacturing technology. Even though AM dates back only to the 1980s, it has developed fast and is maturing towards industrial use [2]. Of the seven technology categories of AM, defined by the ISO/ASTM 52900 standard, powder bed fusion (PBF) with polyamide 12 (PA12) feedstock is considered the most mature category for end-use industrial parts [3]. The two most used technologies under PBF, are selective laser sintering (SLS) and multi jet

fusion (MJF). In both techniques, thermoplastic material in the form of fine spherical powder is heated, consolidated, and solidified layer-by-layer to form three-dimensional objects. Compared to conventional manufacturing methods, AM enables a higher degree of geometrical freedom in part design and manufacture. The added complexity in part geometry translates into opportunities for example in part weight reduction, part consolidation, mass customization, and allows to increase product value [2,4]. The advantages of plastic PBF are the fine feature resolution and ability to produce parts without support structures. The resulting ability to nest the whole build volume with parts and toolless production [2] make plastic PBF an option for injection molding in low to medium volume industrial production [5]. To date, plastic AM parts have been researched and used in numerous applications for example in the medical industry [6,7], in the automotive industry [2], in aerospace applications [8], as spare parts [9], and in

^{*} Corresponding author.

E-mail addresses: tuomas.puttonen@aalto.fi (T. Puttonen), mika.salmi@aalto.fi (M. Salmi), jouni.partanen@aalto.fi (J. Partanen).

<https://doi.org/10.1016/j.polymertesting.2021.107376>

Received 10 July 2021; Received in revised form 2 October 2021; Accepted 8 October 2021

Available online 9 October 2021

0142-9418/© 2021 The Authors. Published by Elsevier Ltd. This is an open access article under the CC BY license (<http://creativecommons.org/licenses/by/4.0/>).

consumer electronics [10]. During the longer existence of injection molding, there has been time to optimize the materials to a stage where even application-specific tailoring of material properties is possible. Instead, a requirement for a wide processing window in PBF limits the material selection to mostly semi-crystalline polymers [5]. In addition, the layer-based manufacturing method is anisotropic. The mechanical properties differ depending on the build orientation and layer thickness [11]. These characteristics, in addition to the lower speed of manufacturing and a need for post-processing to achieve an adequate surface finish, are among the points listed by companies when discussing barriers to wider AM implementation [12]. Nevertheless, many common engineering plastics, such as PE, PP, PS, TPE, PA6, PEK, and PEEK are already commercially available and new materials are constantly in development [11].

In the selective laser sintering (SLS) process, a counter-rotating recoater deposits thin (20–100 μm) layers of fine, spherical material powder which are selectively melted with a heat source, such as a carbon dioxide laser [5]. The alternative PBF technology, multi jet fusion (MJF), deposits liquid fusing and detailing agents with modified inkjet print-heads to selectively control the melting of material on each layer. The heat source in MJF, instead of a point-wise laser, is an infrared lamp affecting a whole layer at a time [13]. The process and material handling influence the local and global material properties [5,11] and the final mechanical properties of a part. In both processes, the build chamber is kept at an elevated temperature during the process. The packing density and diameter distribution of the material powder together with the distribution of energy density will influence the local melting of the material and the resulting microstructure [5]. The process-induced porosity in both techniques results in a less dense part compared to a molded equivalent [14]. The amount of porosity in the MJF process is less pronounced, yet still considerable [15,16]. Nevertheless, cavities, poorly melted powder particles, and overall microstructure anisotropy all affect the mechanical properties and fracture mechanics of plastic manufactured with either of the two processes. In addition, the thermal aging of powder reprocessed for multiple cycles is an element with a connection to material degradation [17]. The aged powder contains more nucleation seeds for the crystallization of lamellar spherulites within the amorphous matrix. Both the tensile strength and elongation at break were found to decrease for single layer parts made with aged powder [18]. A holistic fishbone diagram of material and SLS process conditions that affect the part final properties can be found in Ref. [11].

The shared inferiority of all polymer materials, regardless of the manufacturing technology, is their inherent instability to weathering [19]. Polymers are synthesized via the polymerization of short monomer units to form long chains of even tens of thousands of bonded monomer units [20] and a longer exposure to environmental stress factors such as heat, moisture, oxygen, and ionizing radiation (mostly ultraviolet light) will degrade the structure. Depending on the material and the major environmental contributor of the degradation, the degradation pathways are classified under photo-oxidative degradation, thermal degradation, ozone-induced degradation, mechanochemical degradation, catalytic degradation, and biodegradation [21–24]. To briefly summarize, the essential initiator for photodegradation in polymers is the presence of chromophore groups that absorb sunlight wavelengths in the range of 280–400 nm. The absorbed energy breaks chemical bonds and results in a formation of free radicals. These components, such as alkyl and hydroperoxyl radicals, further react with oxygen, steal hydrogen atoms from the polymer structure, and recombine with other radicals eventually causing a chain reaction of chemical changes in the polymer structure. The process terminates only when radicals or other molecules in the polymer recombine as nonradical, inert components that stop the process [25]. These changes in polymer chain bonds, molecular weight, and composition will deteriorate the mechanical properties of the material, reduce its tensile strength, and cause brittleness. On a directly observable level, the degradation manifests itself as surface discoloration, loss of surface gloss, yellowing, and chalking [26]. Fortunately,

the weathering resistance of materials can be improved by adding photostabilization additives in the bulk material, or via coating, painting, or varnishing of surfaces [27]. Karimi et al. [25] provide an excellent summary of polymer degradation and photostabilization mechanisms. Based on their mode of operation, the additive substances are classified either as UV absorbers, UV screeners, quenchers, antioxidants, nucleating agents, or fillers. UV absorbers and screeners attempt to block the first initiation step of photodegradation by inhibiting UV radiation from reaching the bulk material in the first place. These additives either absorb or reflect the energy. Quenchers convert molecules that have already been excited by the UV energy and passivate them before free radicals would be formed. Antioxidants act later in the chain of events. They terminate the radical chain reactions by rendering their products nonreactive. Nucleating agents and fillers do not directly affect photodegradation but may be used to change material properties like crystallinity and glass transition temperature. Higher crystallinity can, for example, reduce the radical diffusion within the material [25]. A review of the degradation pathways of common engineering plastics is provided in Ref. [1]. The main focus of this paper, polyamide, is considered poorly photostable [28]. UV light at the wavelength of 254 nm can directly break the polyamide C–N bond [29,30]. Radical impurities in polyamide, such as unsaturated carbonyls, contribute in the process. With oxygen and other radical molecules, the impurities will lead to hydroperoxides and an overall cross-linking and chain scission across the material [26,29–31]. In addition, the amide groups render polyamides vulnerable to hydrolysis reactions [28].

The effects of weathering on plastic materials have been studied since the 1950s [19]. Specialized accelerated weathering devices attempt to mimic the relevant environmental parameters for plastic degradation in the laboratory setting. For injection molding and traditionally manufactured materials, studies on the effects of weathering are abundant. To present a few examples, Pérez et al. have investigated consecutive material reprocessing cycles in injection molding and extrusion followed by accelerated weathering tests for polycarbonate [32] and ABS [33]. The number of reprocessing cycles was found to detrimentally affect the tensile strength of the materials in comparison to non-reprocessed samples. The detrimental effect was especially intensified after the accelerated weathering tests. Varsavas and Kaynak [34] report the tensile properties and fracture surfaces after accelerated weathering of injection molded and extruded polylactic acid (PLA) reinforced with 15 wt% glass fiber. An example of stabilized and non-stabilized PA12 after thermal aging is provided in Ref. [35].

However, the knowledge of chemical, microstructural, visual, and mechanical changes in plastic PBF parts due to long-term aging is still limited. The few contributions include a study by Shackelford et al. [26] on the degradation of SLS PA12 in accelerated UVB exposure, the effect of water conditioning on the fracture behavior of PA12 composite [36], heat conditioning of SLS, and injection molded PA12 [31], and high-pressure steam aging of SLS PA12 [37]. As a fairly new technology, the degradation of AM PBF polyamides has been mostly studied from the process perspective to understand heat degradation and the implications of mixing virgin and recycled polyamide powder on the final part properties. Chen et al. [38] investigated the microstructural evolution and chemical changes of SLS PA12 after multiple reprocessing cycles. The effects of different material mixing ratios have been evaluated for the end-part microstructure, properties [18], and final part surface quality [39]. Differences in degradation behavior between the SLS and injection molding processes are studied in Ref. [31]. The after-process mechanical properties of AM PA12 [16,37,40] and glass-reinforced PA12 [41] are extensively covered. However, the fracture mechanics of PBF AM parts are not largely discussed in the literature. The fractures of non-weathered PBF PA12 are briefly assessed in Refs. [40,42]. Liu et al. [43] have attempted a more detailed fracture characterization of SLS PA12 and glass-filled PA12. In a review paper on the fracture behavior of AM parts [44], the focus in plastic parts to date is almost dominantly on material extrusion.

It may be concluded that a better understanding and experimental coverage of the long-term environmental degradation of AM plastics is required. This paper presents a broad dataset and provides a comparative analysis of accelerated weathering effects on the mechanical properties and fracture surfaces of AM PA12 and glass-filled PA12, along with a wide selection of traditionally manufactured engineering plastics. The materials were all tested in the same weathering chamber and similar test conditions to allow comparability. The full experiment data is available for download in the data repository [45]. The samples were studied with a combination of a 1500-h accelerated weathering test (ISO-4982-3) followed by tensile testing (ISO527). All AM samples were manufactured in X and Z build orientations, except for carbon reinforced PA12 (effective reinforcement only in the X build orientation). In addition, two protective coatings were evaluated to compare the mechanical properties and thus weathering resistance between the coated and non-coated samples. The AM PA12 and glass-filled PA12 tensile fracture surfaces were evaluated with scanning electron microscopy to reveal any differences in fracture behavior after the weathering exposure.

2. Materials and methods

2.1. Sample preparation

The tensile test samples were ordered through various suppliers in Europe. The materials, trade names, manufacturing processes, build orientations, and finishes are collected in Table 1. For each studied material type, three samples were exposed to accelerated weathering (weathered) while three reference samples of the same material were kept in a dark cabinet at room temperature (non-weathered). The test specimen dimensions were selected according to the tensile testing ISO-527 standard specimen type “A1”. To ensure rigid clamping to the tensile testing machine, the length of both ends was extended resulting in a total sample length of 190 mm. The 3D model was prepared in CAD software and exported as a high-resolution STL file to retain geometric details of the round between the grip lengths and the gauge length. In addition, a DXF file was prepared for laser cutting or milling of the conventional reference samples. The two build orientations and main sample dimensions are shown in Fig. 1a and b. The thickness of the sample is 4 mm. The SLS parts were manufactured with the EOS P396 (EOS GmbH Electro Optical Systems, Krailling, Germany) with the processing parameters according to the machine provider recommendations. The MJF samples were manufactured with the HP Jet Fusion 4200 (Hewlett-Packard Company, Palo Alto, California, USA) using the “Balanced”- parameter set. The AM parts were de-powdered and dyed black. The applied coating 1 was a common clear spray varnish

commercially available in the hardware store. Coating 1 is alkyd-based and provides basic environmental and chemical protection with a smooth, scratch, and impact-resistant surface. Coating 2 was described as a hydrophobic thin-film coating with similar properties to coating 1 but with the added hydrophobicity of the surface.

2.2. Accelerated weathering

A weathering cycle for the parts was implemented according to the ISO-4982-3 standard in a QUV accelerated weathering tester (Q-Lab Corporation, Westlake, Ohio, USA). The Method “A”, Cycle. No. 1 was selected with fluorescent UVA-340 lamps rated at 0.76 W/m²/340 nm for UV exposure. The test consists of repeating 12-h cycles. An 8-h UV exposure at 60° Celsius is followed by a 4-h condensation phase at 50° Celsius without UV exposure. The total test duration of 1500 h is a combination of 125 12-h cycles. The samples were detached, rotated 180°, and refastened in the middle of the test (750 h) to ensure uniform distribution of UV irradiance on both sides of the samples. 24 custom sample holder plates and rims were designed and manufactured in anodized aluminum. The samples were fastened to the holders with UV-resistant zip-ties and the sample ends were protected with weather-resistant duct tape as seen in Fig. 1c and d.

The accelerated weathering unit comprises a carbon arc, xenon arc, or fluorescent lamps, a heater, humidity control, and sometimes a water spray unit to simulate dew. Carbon arc lamps produce an unrealistic spectrum as compared to natural sunlight with narrow wavelength peaks and emit more on the most harmful UV-C portion of light normally filtered out by the Earth atmosphere. Xenon arc lamps have a good overall correlation with the whole spectrum of natural sunlight but require filtering and active monitoring for lamp decay. Fluorescent lamps do not require as much maintenance and follow closely the lower and higher energy UV-B and UV-A portion of sunlight most often responsible for degradation effects. However, they hardly emit in the wavelengths of visible light that also contribute to the overall degradation [19].

2.3. Tensile testing

The tensile testing of samples was implemented according to ISO-527 standard with a 30 kN MTS Insight tensile testing machine (MTS Systems Corporation, Eden Prairie, Minnesota, USA) at room temperature. The test data was logged with the TestWorks software by the same company. At the beginning of each test, an MTS axial extensometer with a 25 mm gauge length was placed in the middle of the test samples for accurate local strain measurement up to 0.3% extension and further calculation of elastic modulus. Each test was paused for extensometer removal after

Table 1
Sample materials, trade names, manufacturing processes, build orientations, and finishes.

Material ID	Manufacturer, Trade Name	Description	Process	Machine	Orientation	Dye	Coating
PA2200	EOS, PA2200	Polyamide 12	PBF (SLS)	EOS P396	X, and Z	Black	–
PA12	HP, High Reusability PA12	Polyamide 12	PBF (MJF)	HP 4200	X, and Z	Black	–
PA2200	EOS, PA2200	Polyamide 12	PBF (SLS)	EOS P396	X, and Z	Black	coating 1
PA12	HP, High Reusability PA12	Polyamide 12	PBF (MJF)	HP 4200	X, and Z	Black	coating 1
PA2200	EOS, PA2200	Polyamide 12	PBF (SLS)	EOS P396	X, and Z	Black	coating 2
PA3200GF	EOS, PA3200GF	Polyamide 12	PBF (SLS)	Unknown	X, and Z	No	–
Carbon filled and reinforced PA	Markforged, Onyx base with continuous carbon fiber	Glass-filled polyamide 12 reinforced with continuous carbon fiber	Material Extrusion	Markforged Mark Two	X	No	coating 1
ABS Black	ArlaPlast, Atech 3000	Acrylonitrile butadiene styrene	Laser cutting	from sheet	Isotropic	–	–
ABS White	ArlaPlast, Atech 3000	Acrylonitrile butadiene styrene	Laser cutting	from sheet	Isotropic	–	–
PC UV	Covestro, Makrolon UV	UV-treated Polycarbonate	Laser cutting	from sheet	Isotropic	–	–
PMMA	Plazit Polygal, Plazcast-led	Poly (methyl methacrylate)	Laser cutting	from sheet	Isotropic	–	–
PA66GF30	Ensinger, Tecamid 66 GF30 Black	30% Glass-filled polyamide 66	Milling	from sheet	Isotropic	–	–
PA66MoS2	Ensinger, Tecamid 66 MO Black	Molybdenum disulfide polyamide 66	Milling	from sheet	Isotropic	–	–
PA12G	Ensinger, Tecamid 12	Cast polyamide 12	Milling	from sheet	Isotropic	–	–

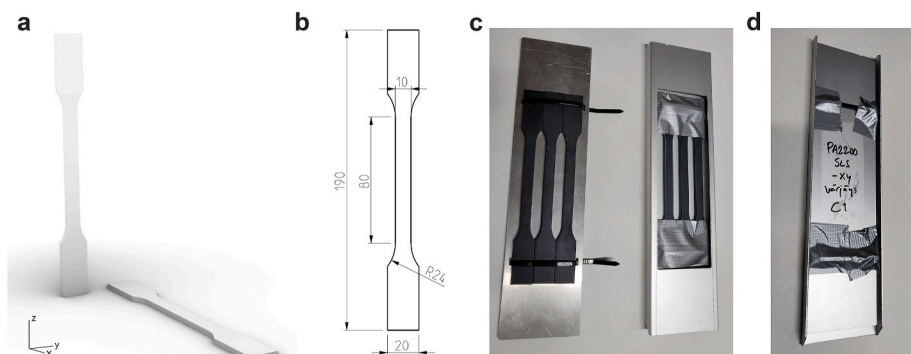


Fig. 1. Tensile sample build orientations, dimensions, and QUV holder design. a) Build orientations Z and X, b) main sample dimensions, and c) and d): QUV holder assembly samples attached seen from the front and from the back.

which the test was continued until sample failure. Throughout the test, load, tensile stress, crosshead displacement, and extensometer data were collected. The thickness and width of each sample were measured with a manual caliper as an average of three measurements. The logging frequency of values was kept at 20 Hz and the testing speed generally at 2 mm/min. The same operator was responsible for all the tests.

The data of each tensile test was exported as a CSV file. The elastic modulus, ultimate tensile strength, and crosshead displacement of each sample were calculated and plotted with a custom python script (with pandas, NumPy, and matplotlib libraries). The averages and standard deviations of the sample sets were calculated with the Python statistics package. For each set of three samples, a polynomial curve was fitted into the data points to visualize average material behavior.

2.4. Fracture surface analysis

The fracture surfaces of SLS PA12 and glass-filled PA12 were further evaluated with scanning electron microscopy (SEM). A conductive 4 nm thick layer of platinum/palladium was applied to the sample surface with a Leica EM ACE600 sputter coater (Leica Microsystems AG, Wetzlar, Germany). The images were acquired using a Zeiss Sigma VP SEM

(Carl Zeiss AG, Oberkochen, Germany) with the SE2 detector and 5 kV target accelerating voltage. The individual images with an identical magnification were processed and stitched as panoramas with the open-source ImageJ/Fiji software and a plugin by Stephan Preibisch et al. [46].

The sample geometry 3D models, QUV sample holder manufacturing files, the Python script, and all original CSV files are provided in the dataset for research reproducibility [45].

3. Results and discussion

3.1. Overview of mechanical properties

120 samples and a total of nine materials provide a large reference dataset of mechanical behavior before and after accelerated weathering. Table 2 presents the average values and deviations of three samples before (non-weathered) and after accelerated weathering (weathered), including ultimate tensile strength, elongation at break, and elastic modulus. Relative percentual changes have been calculated between the non-weathered and the weathered values. X and Z denote the build orientation for samples manufactured with AM. Samples with an applied

Table 2

Average values of three samples for ultimate tensile strength, elongation at break, and elastic modulus including sample standard deviations (SD) of all tested samples; non-weathered, weathered, and relative changes in percentage. AM build orientations are compared to the non-weathered sample average. The values compared to are highlighted in blue.

Sample	Non-Weathered Samples					Weathered Samples					Relative Change				
	Tensile Strength (Mpa)	SD	Elongation at break (%)	SD	Modulus (Mpa)	SD	Strength (Mpa)	SD	Elongation at break (%)	SD	Modulus (Mpa)	SD	Δ% Stress	Δ% Elongation	Δ% Modulus
PA2200 X	46.62	0.63	11.94	0.14	1852.51	35.16	29.11	0.53	1.25	0.04	1795.60	13.21	-37.56	-89.55	-3.07
PA2200 X coating 1	41.57	3.86	4.59	3.92	1857.08	11.58	44.28	1.93	6.28	2.34	1865.33	1.47	-5.00	-47.42	0.69
PA2200 X coating 2	42.64	0.38	7.08	0.36	1776.25	25.17	38.51	1.18	3.97	0.56	1606.90	26.56	-17.39	-66.78	-13.26
PA2200 Z	45.57	0.20	6.56	0.18	1886.50	67.13	33.84	1.13	1.76	0.15	1799.42	40.56	-25.74	-73.16	-4.62
PA2200 Z coating 1	41.28	3.90	4.48	2.28	1938.09	14.70	42.98	0.90	4.67	0.58	1950.95	50.71	-5.70	-28.84	3.42
PA2200 Z coating 2	38.71	1.68	2.60	0.41	1780.32	14.79	36.23	0.80	2.35	0.21	1713.37	23.94	-20.50	-64.11	-9.18
PA12 X	37.27	3.60	7.88	1.65	1350.20	108.18	19.77	0.93	1.21	0.10	1337.21	34.98	-46.95	-84.61	-0.96
PA12 X coating 1	30.90	5.74	3.72	2.94	1429.12	88.96	35.04	2.59	4.10	1.10	1450.17	67.73	-5.98	-48.00	7.40
PA12 Z	46.16	2.85	8.31	3.97	1831.88	49.02	23.22	1.30	1.02	0.08	1745.81	30.06	-49.69	-87.69	-4.70
PA12 Z coating 1	34.92	2.22	1.82	0.26	1794.33	29.32	35.22	6.46	2.67	1.63	1768.48	44.36	-23.70	-67.90	-3.46
PA3200GF X	29.86	1.96	2.61	0.89	3267.98	333.94	22.37	2.50	2.79	0.06	2789.53	76.22	-25.09	7.08	-14.64
PA3200GF Z	25.34	4.80	1.47	0.19	2785.78	303.01	22.24	2.32	1.86	0.13	2397.88	174.58	-12.23	26.54	-13.92
Carbon filled and reinforced PA	155.04	5.01	1.65	0.10	16555.19	154.12	160.21	9.43	1.66	0.05	16690.69	309.45	3.33	1.12	0.82
PC UV	63.82	0.23	50.70	3.25	2432.93	32.37	64.01	0.33	6.38	0.84	2444.79	57.02	0.29	-87.41	0.49
PMMA	71.27	1.69	3.26	1.02	3316.80	31.98	53.89	8.25	1.42	0.36	3242.51	69.19	-24.36	56.28	-2.24
ABS Black	29.37	0.03	7.59	1.42	2076.21	26.73	28.86	0.08	3.55	0.22	2119.12	31.71	-1.73	-53.30	2.07
ABS White	35.68	0.64	4.11	1.47	2227.85	111.87	33.66	0.19	1.39	0.06	2350.59	5.92	-5.66	-66.06	5.51
PA66GF30	64.85	1.30	5.94	0.43	3595.17	121.98	51.53	0.47	8.38	0.24	2386.58	44.27	-20.54	41.20	-33.62
PA66MoS2	67.12	0.42	24.94	1.47	3012.95	399.49	55.76	2.48	17.27	2.60	1943.18	490.87	-16.93	-30.75	-35.53
PA12G	60.13	2.73	174.00	10.41	1760.50	23.26	36.04	2.31	2.59	0.97	1556.91	80.00	-40.07	-98.51	-11.58

coating were compared to a non-coated reference to assess how the coating affected the mechanical properties.

The tensile testing results with and without weathering reproduce the already well-known observation of an increased material brittleness after weathering across a wide range of materials [19]. Even though the polymer weathering-induced embrittlement has become an empirically known fact, the microstructural reasons behind the ductile-brittle transition are still not fully understood. The chemical changes that contribute to microcracking and embrittlement of a bulk material are related to chain scission, crosslinking, and crystallinity changes in the material. Material ductility has been explained to link with chain entanglement, molecular forces such as hydrogen bonds and van der Waals forces, and the amorphous phase chain drawing [47]. The chain

scission and lower adhesion forces in the interlamellar space become initiation sites for microcracks as mechanical stress is applied [48].

Polymer weathering in amorphous polymers progresses via chain scission which decreases the molar mass, breaks the entanglement networks between polymer chains, and leads to the overall embrittlement of the material. A critical threshold of molar mass can be identified above which the material behavior is always ductile [49]. The semi-crystalline polymers, such as polyamides, do not behave as routinely. The crystalline morphology plays a role in the failure mechanisms [47]. The crystal lamellae in weathering thicken via a process called chemi-crystallization. The chain fragments from scission in the amorphous phase may recombine with the crystalline phase. The embrittlement in semi-crystalline polymers has been proposed to link

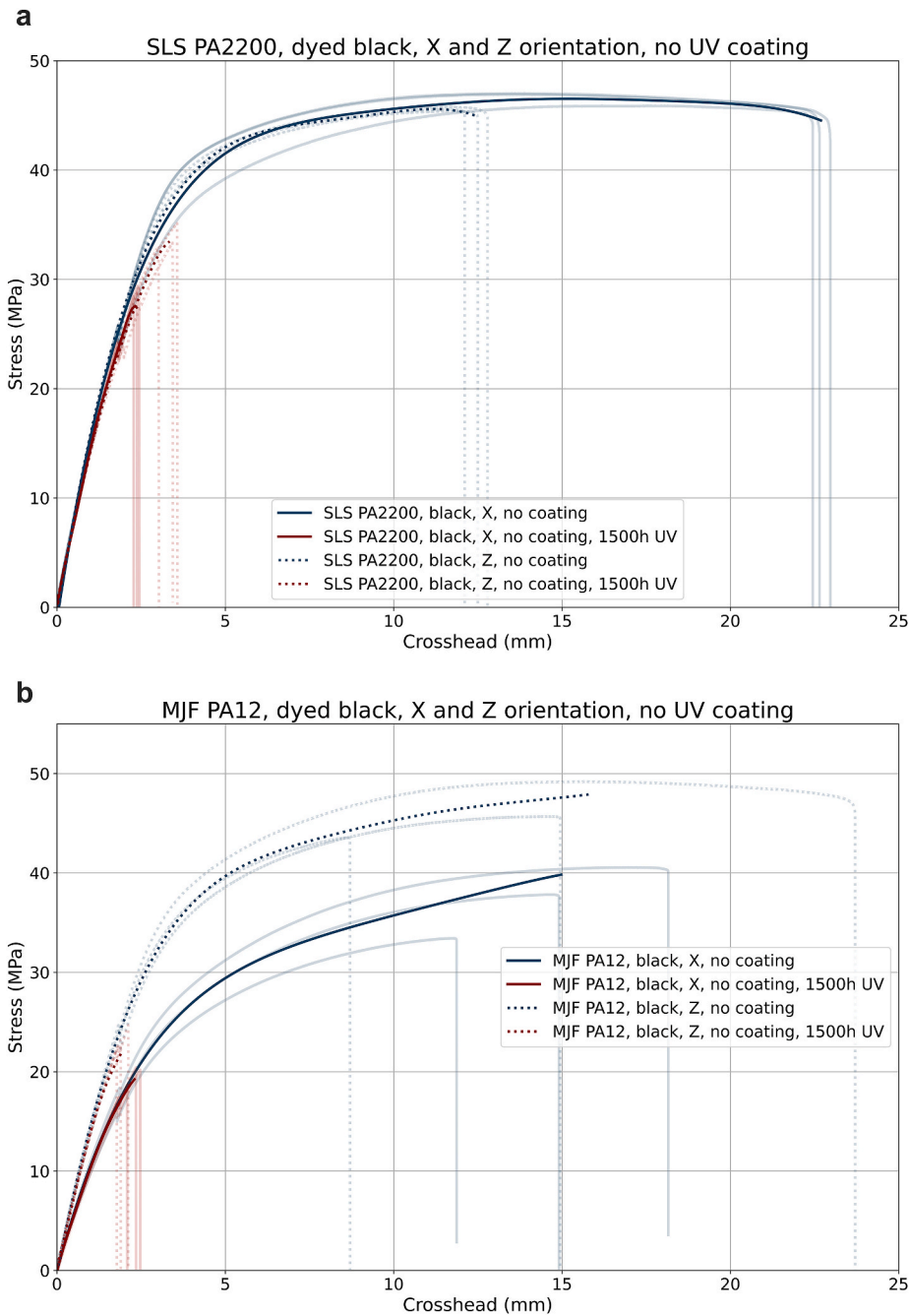


Fig. 2. Tensile test stress-crosshead displacement graphs for AM PA12. Manufactured in X and Z build orientations without UV coating with a) the SLS process and b) the MJF process. The opaque curves represent polynomial fits calculated from the individual test sample data shown with translucent lines. The non-weathered samples are colored blue while the weathered series is shown in red.

with decrease of entanglement in the amorphous phase (as with amorphous polymers), loss of tie molecules, and shrinking of the interlamellar distance between crystals [49].

The relative change of elongation at break was prominent for all non-treated polyamides, polycarbonate, and cast polyamide 12. With the largest reductions in ultimate tensile strength, non-treated polyamides were the most sensitive material to weathering in the test set. The change in elastic modulus, for most materials, is less pronounced than the changes in tensile strength and elongation at break. With most materials, it could be attributed entirely to test noise. The only significant changes in elastic modulus occurred for reinforced materials, filled PA12 and PA66 reinforced with either glass or molybdenum disulfide. Interestingly, both glass-filled materials became more ductile because of weathering. This observation was further studied via SEM of the fracture surfaces. The applied coatings, and especially UV stabilizers or additives already administered as part of the plastic compound reduce brittleness and minimize changes in the material behavior. This was most clearly visualized with UV-treated polycarbonate which retained its peak stress value and modulus albeit becoming considerably more brittle.

Each tensile-tested material series is accompanied by a full stress-crosshead displacement plot to material failure with non-weathered and weathered samples and manufacturing orientations. Fig. 2 displays an example. The tensile strength, elongation, and modulus values, in some cases, differed from the values denoted in the official material datasheets. These differences are not extensively unraveled here. Full data for all materials together with stress-crosshead displacement plots, standard deviations, and pictures are made available in the dataset [45].

3.2. Additive manufacturing plastics

The ultimate tensile strength for non-coated AM PA12 decreased on average 40% and the elongation at break value 84%. Only the carbon-filled and reinforced PA with a UV varnish did not experience a significant change in mechanical properties after the weathering cycle. In general, the reduction of mechanical properties was more pronounced for non-coated AM and cast PA12 signaling an inherently inferior weathering performance of polyamide compared to the other tested materials.

The detailed stress-crosshead displacement plots visualize the whole material behavior up to material failure for each of the three samples in a material category. As can be seen in Fig. 2, individual stress-crosshead displacement curves are visualized in translucency and the opaque curve denotes a polynomial fit to all the data points of a material category. Only the polynomial fit curves will be used to visualize the average material behavior in subsequent images to maximize visual readability.

3.2.1. Non-weathered samples, build orientation and process differences between SLS and MJF

The stress-crosshead displacement plot in Fig. 2a demonstrates that a well-calibrated SLS machine can produce uniform parts with very low variation between samples. The average tensile strength for the SLS parts was in the range of 45–46 MPa. The Z build orientation values are close to that of the X orientation. However, a clear reduction of average crosshead displacement is observed between the build orientations with an average of 23 mm for the X orientation down to 13 mm for the Z orientation, in agreement with the material datasheet. The average elastic modulus was 1796 MPa for the X direction and 1799 MPa for the Z orientation which are higher than the values stated in the datasheet, 1650 MPa for both orientations.

Calignato et al. [16] provide tensile testing results for PA12 according to the ISO 527 standard for both SLS and MJF processes manufactured in a total of nine different build orientations. The reported values for tensile strength are approximately 10 MPa lower than the values acquired in this study. The study reports a higher elastic modulus for the X orientation samples compared to the Z orientation which was not reproduced here. The clear difference in elongation between the X

and Z orientations agrees with the results. The reported SLS values by Rosso et al. [40] for Z orientation tensile strength and tensile modulus are in close agreement.

As seen in Fig. 2b, the variation of mechanical properties for the MJF manufactured samples was more distinct for both ultimate tensile strength and elongation at break compared to the SLS. A very clear difference in elastic modulus was also observed between the two MJF build orientations. The average tensile modulus for the X direction was 1350 MPa and for the Z direction 1832 MPa. In the datasheet of MJF PA12, the difference is expected. However, the observed variation was more distinct. In contrast to the results acquired here, Connor and Dowling [42] have reported very low deviation and close to isotropic results for parts made with MJF in X, Y, and Z orientations. Rosso et al. [40] also report low deviation, albeit only for the Z build orientation. The reported properties for MJF by Calignato et al. [16] are in better agreement with the results of this study. Both tensile strength and elastic modulus are, on average, highest in the Z orientation. However, the elastic modulus values do display high standard deviations. As with the results of this study, high deviations for elongation render an accurate comparison between orientations impossible.

The limitation of only three samples per material category and deviations of values are to be noted when assessing the results of this study. The large difference in modulus and deviation of mechanical properties across samples could be attributed to machine calibration, environmental factors such as temperature and humidity, the mixing ratio of aged and virgin powder, and powder handling. These would require individual-specific studies. Rosso et al. [40] have reviewed the literature for tensile test data on SLS and MJF and collected the values for comparison. All the studies highlighted here employed an HP MJF 4200 machine with a “Balanced”- parameter set. A wide design of experiments study with equivalent machines, settings, and process steps would be needed to accurately assess the variation of mechanical properties to further identify the reasons for variation.

The SEM pictures in Fig. 3 display the fracture surfaces of the AM non-weathered samples in X and Z build orientation. All SEM images were taken from the samples manufactured with the SLS process. In X orientation, images a) and b), layers are running towards the observer. In Z orientation, images c) and d), layers are perpendicular to the observer. The overview pictures with a modest magnification cover a fracture area of approximately 1.8×1.2 mm while the full sample cross-section is by design 4×10 mm. The fracture surface topography does not clearly distinguish layer interfaces or individual laser hatch lines. Material delamination in Fig. 3a is not explained by the layer direction as layers run perpendicular to the observed delamination. In all SEM images of the AM materials, notable is the high frequency and size of material porosity. The cavities range up to more than a hundred micrometers in diameter. The cavities comprise unmolten, or partially melted particles best visualized in Fig. 3c. In addition, a high occurrence of defects, microcracks, and unmolten particles at or near the surface along with material discontinuities is observed. Both build orientations include fracture features that indicate brittle (Fig. 3, left column) and ductile (Fig. 3, right column) local material behavior. Zones of finer ductile behavior near the sample surface are annotated in Fig. 3b and d. The location of microductility indicates a slower material yielding has initiated from surface defects and increased in speed as moving in the overall direction of the ductile fracture lines and finally transitioning into a dominantly brittle fracture. Areas with ductile fracture features appear to be, on average, more porous. This is natural as higher stress concentrations would occur at the sites with the least cross-sectional material. The interfacial yielding between unmolten and completely melted material was observed to occur only on very small scales, yet may play a role in the crack initiation as proposed by Liu et al. [43]. However, the overall ductility and elongation of the material are linked to the areas with apparent microductile and ductile behavior as seen in Fig. 3b and d. The proportion of these features is considerably more dominant than microductility at the interfaces.

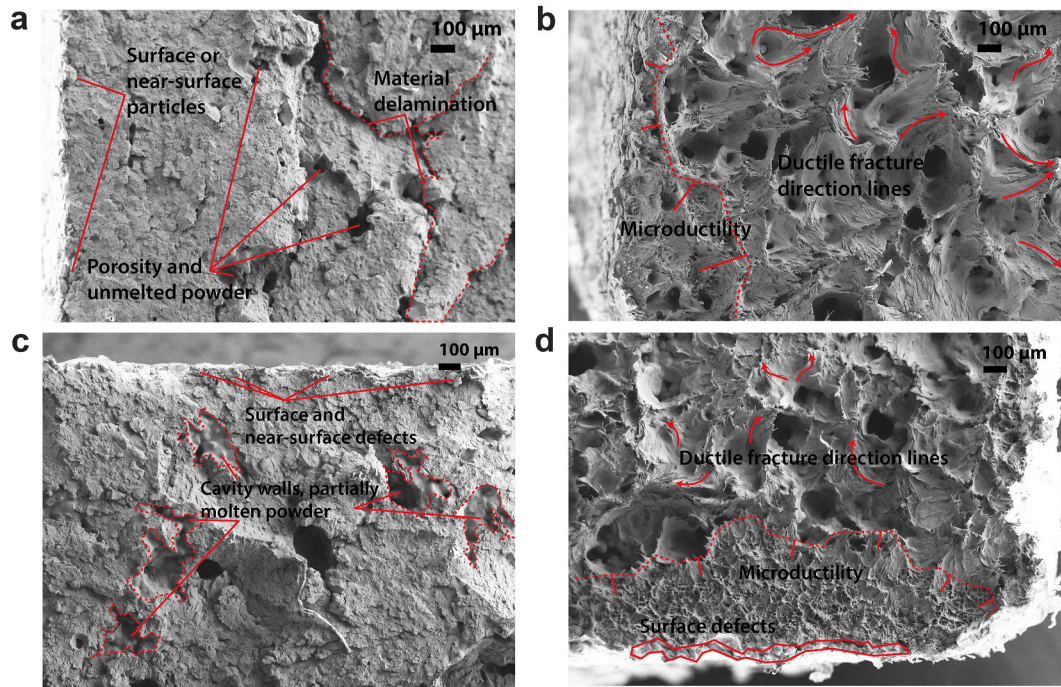


Fig. 3. Overview SEM pictures of the fracture surfaces of non-weathered samples. All scale bars are 100 μm . a) and b): locations from the same SLS sample manufactured in the X build orientation. c) and d): locations from the same SLS sample in the Z build orientation.

In other studies, the fracture features of SLS samples were dominantly brittle as observed by Rosso et al. [40]. In contrast, the Z orientation sample studied here did exhibit local microductility and ductile behavior. Seltzer et al. [36] assess the failure of PA12 to be because of microfibrillation and semi-brittle behavior. However, the build orientation was not defined in their study. Liu et al. [43] have more thoroughly analyzed the fracture surfaces of both AM PA12 and glass-filled PA12. They concluded that the fracture origin for PA12 lies in the different mechanical properties of unmolten and completely melted material. The microductility at the interface is promoted as the cause for overall material toughness and initial crack growth. Based on the SEM images obtained in this study, a connection between poorly, or completely unmolten and melted volumes may indeed play a role in the fracture dynamics. However, a definite conclusion would require a dynamic test setup possibly with digital image correlation (DIC) or via in-situ testing and time lapses using μCT or synchrotron tomography as in Ref. [48]. In addition, a study is suggested where laser energy density is deliberately adjusted to produce and study the failure mechanisms of such an interface.

The shape and spatial arrangement of porosity for SLS and MJF PA12 samples have been examined with x-ray microcomputed tomography

(μCT) in a few studies. Calignato et al. [16] found the porosity of SLS samples higher compared to MJF. The pore shape between technologies was reported as similar. However, the coarse voxel size of 74 μm in the study renders identification and analysis of pores smaller than approximately 200 μm infeasible [50]. Sindinger et al. [15] studied the effect of sample thickness on mechanical properties and pore distribution. A finer voxel size of 10 μm provides a better resolution for smaller pores. They reported the maximum size of pores increases with increasing sample thickness. A clear difference in porosity was revealed between the shell and the core material. Most pores are classified as granules rather than spheres as their mean sphericity ranges from 0.5 to 0.55 in the two studies, a value of 1 denoting a perfectly spherical shape. These observations are consistent with the SEM images obtained here, especially seen in Fig. 7. The shell regions, approximately 300 μm from the sample surface, are consistently less porous than the inner core material. Battu et al. [37] characterized even smaller pores with a synchrotron x-ray source and a voxel size of 1.3 μm .

Fig. 4 shows a magnified view of the brittle fracture surfaces. Fig. 4a presents a surface closer to the sample surface whereas in Fig. 4b the surface is located closer to the middle of the fracture surface plane, at a distance of 1500 μm . Both of the SEM images were taken from the same

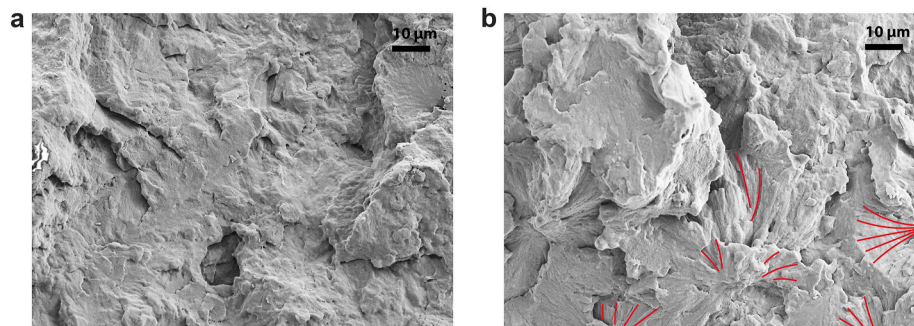


Fig. 4. Detailed SEM images of brittle fracture surfaces in a non-weathered X build orientation sample. Both scale bars are 10 μm in length. a) A site at a 200 μm distance from the sample surface and b) a site at a 1500 μm distance from the sample surface.

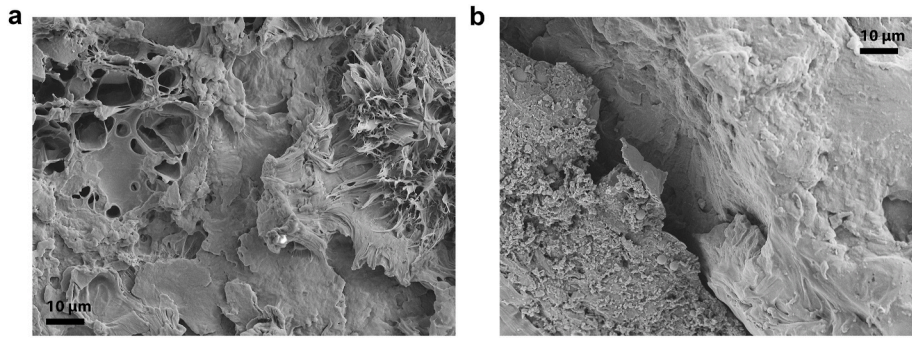


Fig. 5. Detailed SEM images of fracture features. a) Microductility observed in a non-weathered Z build orientation sample with the coating 1 and b) a microporous zone with loose unmolten particles from a non-weathered sample in X build orientation and coating 1. Scale bars in both images are 10 µm.

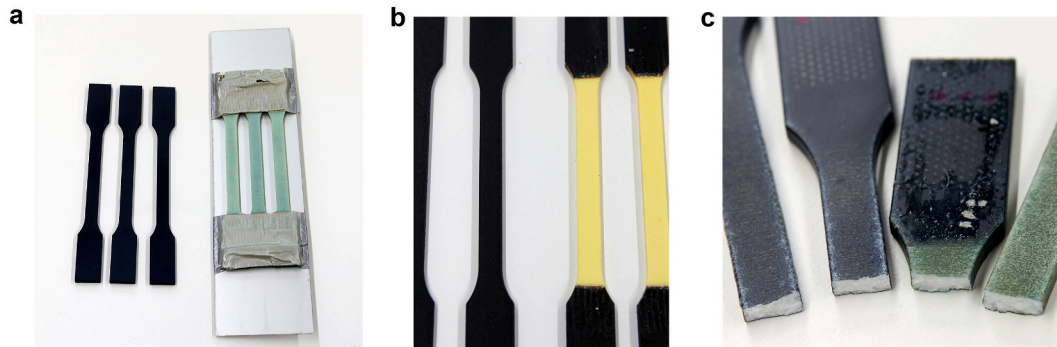


Fig. 6. Color fading and discoloration between non-weathered and weathered samples. a) comparison of non-weathered and weathered samples, b) discoloration of SLS PA12 samples with coating 2, and c) close-up image of the fractured non-weathered and weathered SLS PA12 sample with coating 1.

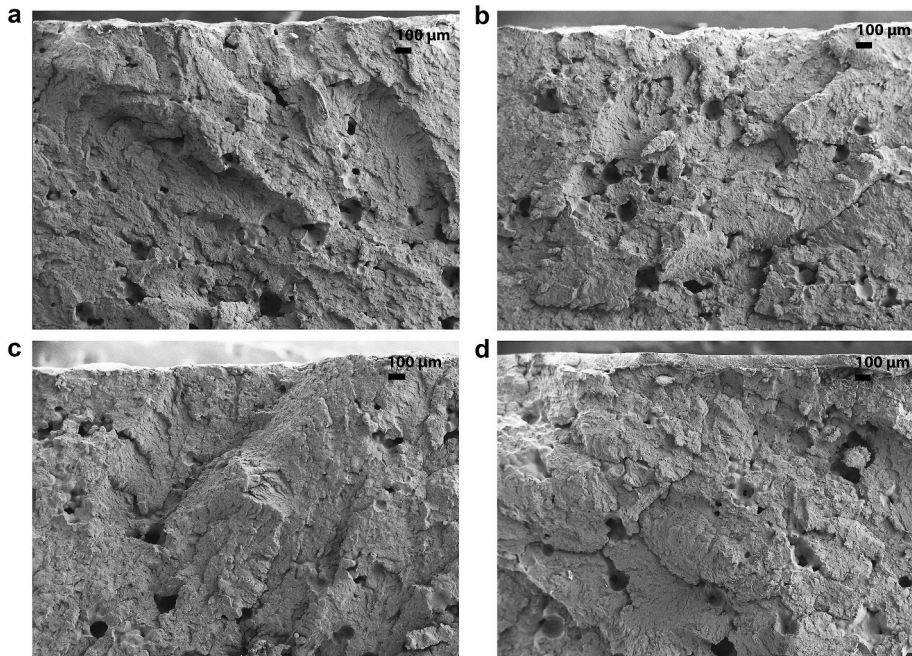


Fig. 7. Overview SEM images of the weathered SLS PA12 samples without UV coating and with coating 1. All scale bars are 100 µm in length. a) X build orientation without coating, b) X build orientation with coating 1, c) Z build orientation without coating, and d) Z build orientation with coating 1.

non-weathered sample manufactured in the X build orientation yet provide a very representative morphology of the brittle fracture surfaces found in all the studied AM PA12 samples. In Fig. 4b, the red annotations mark radially emanating spherulite lamellae also seen in Fig. 8a and b. The panorama SEM images found in the dataset provide a more holistic,

lower magnification visualization of this arrangement. The crystallinity and number of nucleation seeds for spherulites increase with more aged PA12 powder in the AM process [18,39] A crack is more likely to initiate from the spherulites [51] rather than the amorphous matrix.

Another set of higher magnification images in Fig. 5 display a few

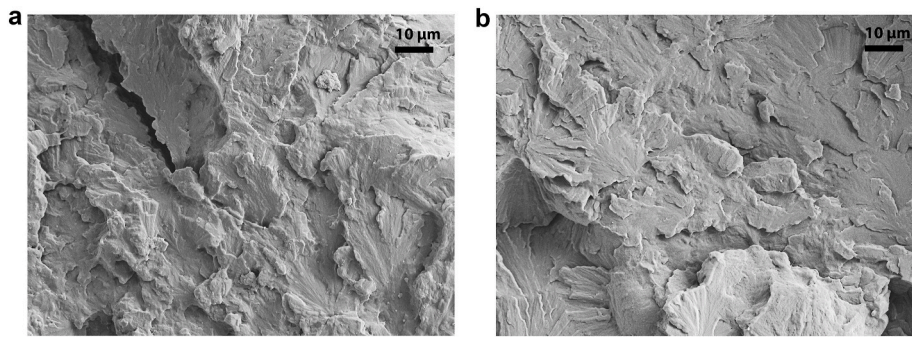


Fig. 8. Detailed SEM images of the brittle fracture surfaces in a weathered X build orientation sample. Both scale bars are 10 μm in length. a) A site at a 200 μm distance from the sample surface, and b) a site of 1300 μm distance from the sample surface.

fracture features which were not presented in previous images. Fig. 5a is a magnified view of local microductility 200 μm from the sample surface in a non-weathered, coated sample manufactured in the Z build orientation. Fig. 5b shows a peculiar microporous zone that was a more rare fracture topography. This time from a coated, non-weathered sample made in the X build orientation. Note also the spherical particles approximately 2–4 μm in diameter.

3.2.2. Weathered samples and UV coating

Clear thin-film coatings are employed for environmental material protection where optical transparency is desired, for example on wood paneling to reveal the aesthetic beauty of the surface [52] or on metal surfaces to better resist corrosive environments [53]. In the context of polymer protection against weathering, such coating provides a barrier against direct water absorption, reduces oxygen diffusion, inhibits surface erosion, and absorbs or scatters a portion of harmful radiation. These combined effects retard the degradation of the underlying material.

The exposure in accelerated weathering greatly reduces the ultimate tensile strength and elongation at break values as seen both in the stress-crosshead displacement graphs in Fig. 2 and Table 2. The elastic modulus was not found to deviate significantly after weathering. The severity of degradation was reduced with coatings of which the overall performance of coating 1 was better. Coating 1 did not significantly alter elastic modulus whereas an average relative reduction of 11% was observed for samples where coating 2 was applied. For both coatings, deviations in mechanical properties were intensified compared to the non-coated samples. The effect was more pronounced for coating 1.

The chemical and microstructural changes which affect mechanical properties were presented in the beginning of Section 3.1. In agreement to previous studies with PA6 [48], PA12 [26], and PE [47], and PC [54], the elastic modulus after weathering was found to alter very little compared to the drastic changes in ultimate tensile strength and especially the reduction in elongation at break. In comparison to the long 1500-h test cycle presented in this article, embrittlement in a similar accelerated weathering setup for polyamide 6 was visible already after less than 100 h of testing. The mechanical response did not change regardless of the aging condition up to 192 h of testing [48]. Based on the results in this paper, no clear difference for PA12 was found even after 1500 h of testing. In contrast to bulk specimen, the thin films (100 μm) displayed strain hardening with lower UV doses (48 h) before subsequent material weakening. However, even if the thin material film photo-oxidated throughout, no change in elastic modulus was reported [48]. This suggests the molecular changes will not significantly affect the immediate material behavior in tensile stress even if the whole bulk of the material is degraded. As proposed by Ref. [26], the molecular changes would only ease the formation of cracks when the material enters yield and cause embrittlement and reduction in tensile strength. For some materials like PP [55], phenoxy resins, and acrylate-melamine thermosets [56], the elastic modulus in weathering was found to

increase. The change in modulus is explained by the competition of material chain scission and crosslinking during aging [56].

The discoloration of parts was visually assessed, and the dataset [45] provides photographs of all sample materials before and after testing. All AM PA12 parts were dyed black and experienced a varying amount of color fading and discoloration after the weathering cycle. Fig. 4 provides an overview of the color changes. Coating 1 did reduce discoloration whereas coating 2, surprisingly, seemed to act as a discoloration catalyst. The post-weathered surfaces with coating 2 experienced aggressive yellowing as seen in Fig. 6b. The elevated temperature in accelerated testing (60 $^{\circ}\text{C}$) may catalyze chemical reactions that would not occur in the same timescales in natural weathering. The dye thickness, as seen in Fig. 6c, is only in the order of a few hundred micrometers. With the rough surface structure, degraded dyed particles can more easily erode from the surface. The discoloration in outdoor applications would be further intensified by rain. A coating provides a mechanical stabilization to erosive effects.

In the MJF process, the fusing agent that promotes the absorption of infrared energy contains graphitic carbon (5.2%) that remains in the finished part [16]. Even though carbon black is considered a photostabilizing element [25], it did not have a measurable effect on the weathering resistance of the tested parts when compared to SLS. Visually, the MJF parts did retain their black color better as the inherent gray color caused by the carbon content promotes the efficiency of the black dye. However, this feature of MJF also restricts the use of the whole RAL color spectrum.

Both the absorption of photons and oxygen diffusion are affected by the specimen thickness [48]. In lower temperatures, the oxidation of the bulk material over time is more uniform, but still existent. In some cases of high-temperature oxidation tests, the oxidized skin of a sample may be as thin as 100 μm . Depending on the photo-oxidation depth, the resulting structure may become a composite with an embrittled surface layer (affected more by weathering), and a ductile material core that has retained the original material properties [57]. The oxygen permeability of polyamides is low [29] yet their chemical structure is also highly susceptible to oxidation [57].

The effects of accelerated weathering were hypothesized to manifest as changes in the fracture surfaces and possibly via gradient changes in the microstructure moving deeper into the bulk of the material. Comparing the detailed SEM images from non-weathered samples in Fig. 3 and weathered surfaces from Fig. 7, such distinction can not be made. In addition, Fig. 8 compares the surface morphology near sample surface (200 μm) and closer to the centerline of the 4 mm thick specimen (1300 μm). No clear difference in fracture surface morphology or an aging gradient with increasing material depth could be identified. A higher magnification research method and chemical assessment is required. Recently, Shackelford et al. have studied the nanoscale changes occurring at the part surface after UVB exposure with monoenergetic positron spectroscopy and suggested that the near-surface structure alterations due to accelerated weathering play a role in the

reduction of mechanical properties [26]. However, more studies of the degradation penetration depth and effect of build orientation are proposed. The cutting of samples at different depth intervals combined with an analysis for chemical and microstructural changes is suggested. The machining of degraded surfaces at different depths in combination with tensile testing and fracture analysis could be another approach.

In the SEM images of coating 1 in Fig. 7d, thickness is on average 100 μm and introduces an additional discontinuity at the interface of base material and zone affected by the coating. The properties of the material may be locally affected by the coating or induce residual stresses at the material interface. These differences may act as artificial fracture initiation sites in tensile testing and explain the larger deviation of mechanical properties between the non-coated and coated samples.

The protective performance of a clear, transparent coating is poor in comparison to opaque paint systems because of a lack of pigment that would efficiently absorb UV light [52]. The weathering performance of a clear coating may be improved with stabilization substances such as UV absorbers or quenchers, such as HALS [58] or the addition of nanosized particles [53,59]. Because the film is thin, the amount of stabilization substances is low, and they are consumed fast by photo-oxidation. As a result, current clear coating technology may only provide protection for a few years in outdoor applications [52].

3.2.3. Weathered and non-weathered glass-filled polyamide

Again, Table 2 provides the mechanical properties and relative changes of non-weathered and weathered glass-filled PA12. Peculiar to all glass-filled test samples was the increase in ductility for the weathered samples. Similar behavior was seen in glass-filled polyamide 12 made with SLS as well as cast glass-filled PA66. No clear difference in fracture mechanism was identified between the non-weathered and weathered SLS samples. The overall microstructure is a matrix of PA12 with a 40% volume fill of glass beads of approximately 50 μm in diameter. Fig. 9 displays a non-weathered and a weathered fracture surface both manufactured in the X build orientation. The consistent

diameter, a deviation within 10 μm , and sphericity of individual glass beads are seen in Fig. 9b and further magnified in Fig. 9d. There were no clear visually distinguishable differences in glass bead form, surface structure, or surface residuals before or after weathering.

Both non-weathered and weathered fracture surfaces comprised of features typical for brittle and ductile fracture. Fig. 9c provides an overall view of such an interface. The upper left portion of the image displays a local area with apparent ductility of the base material transitioning to a dominantly brittle failure on the right. Ductile failure occurs via the base material yielding around the glass particles as best seen in Fig. 9b. In Fig. 9d a minor gap in interfacial bonding is seen between PA12 base material around the glass beads, which may explain the increase in ductility after weathering. Visually, a higher proportion of glass beads has detached from the matrix when comparing the weathered and the non-weathered samples in Fig. 9 but a statistical assessment would be required.

The observation of the behavior of glass-filled materials in accelerated weathering is an interesting finding. Based on results on the virgin PA12, nylon itself becomes more brittle in weathering. Glass, on the other hand, is considered inert against changes induced by UV radiation, moisture, and the temperature range in accelerated weathering. Thus, the change in ductility must be attributed to the bonding between glass beads and the base material. At the tensile stress and ductile fracture sites, the polyamide stretches around the glass beads as seen in the detailed SEM image in Fig. 9b. With an interfacial gap between the matrix and the glass beads after weathering, this interlaced movement may become easier and explain the increase in ductility.

In a study of accelerated weathering of glass fiber reinforced epoxy, changes in interfacial bonding between the epoxy matrix and glass fiber strands were proposed as the reason for changes in the mechanical behavior [60]. Seltzer et al. [36] assessed good bonding between the matrix and the glass beads based on the matrix material residue seen on the bead surfaces in the SEM images. O'Connor et al. [42] instead, reported poor bonding based on visual assessment and void sites of

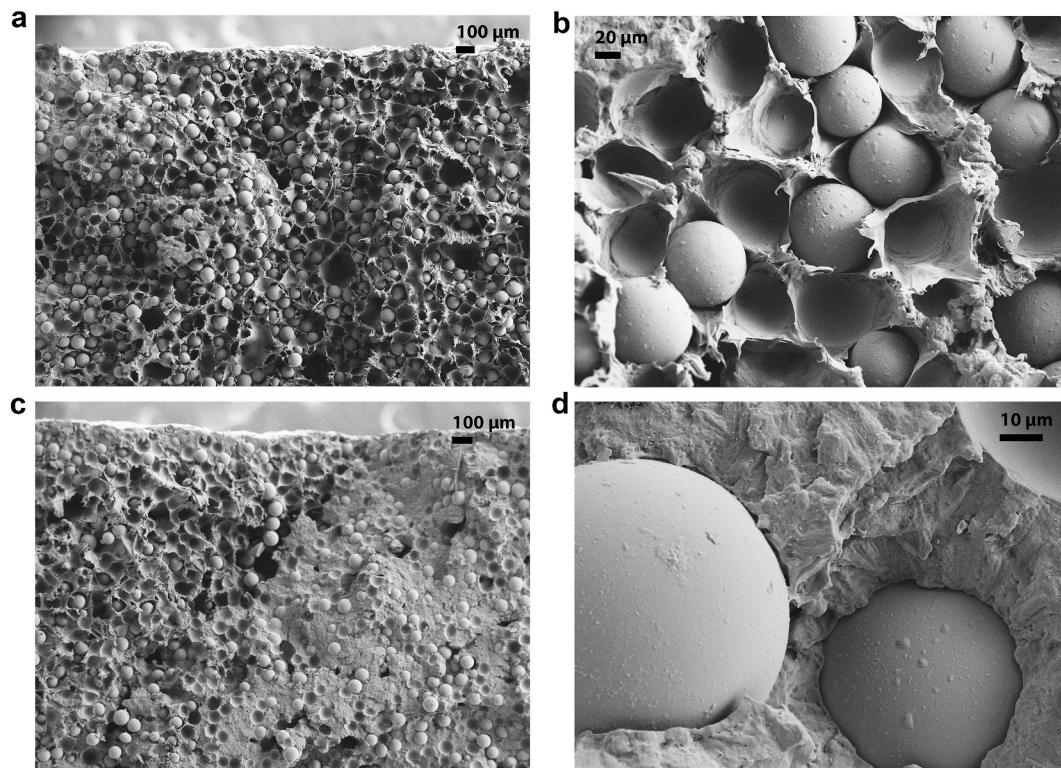


Fig. 9. Overview and detailed SEM images on the fracture surfaces of glass-filled PA12 manufactured with SLS. a) and b): non-weathered sample manufactured in X build orientation. c) and d): weathered sample in X build orientation.

dislodged glass beads. Liu et al. [43] attained a similar conclusion, as well as Lanzl et al. [41]. In the SEM images obtained here, minor residuals are visible, but they are not distinguishable between the weathered and the non-weathered samples. A non-subjective assessment to study this phenomenon would be beneficial.

3.3. Conventional materials

Table 2 provides the average behavior of non-weathered and weathered reference samples made with conventional engineering plastics and processes. The tested materials were polycarbonate (PC), Poly (methyl methacrylate) (PMMA), Acrylonitrile butadiene styrene (ABS) in white and black, glass-filled polyamide 66, molybdenum disulfide-filled polyamide 66, and cast polyamide 12. Fig. 10 displays the material behavior with polynomial fits of each data series.

PMMA is inherently considered a weather-resistant polymer type. The PC in this series was UV stabilized. Albeit the brittleness and reduction of ultimate tensile strength for PMMA, PC, and ABS, these materials retain their elastic modulus after weathering and follow a very similar stress-strain curve up to a material failure. The filled materials, glass-filled and molybdenum disulfide-filled PA66, experienced a considerable reduction in elastic modulus. It is to be noted that the tested materials were not oven-dried after the accelerated weathering tests. Absorption of moisture reversibly affects the elastic modulus [36, 61]. However, the low modulus changes with PA12 and the fact that glass-filled polyamide 12 exhibited a similar trend rules out moisture as the only explanation. Interestingly even with the same matrix material, the change in the ductility of the two materials is reversed. This indicates a considerable difference in the behavior of the two reinforcement particles in relation to the PA66 matrix in tensile stress. Dynamic experimental methods are suggested to further study this phenomenon. The black pigment of ABS was found to slightly increase the material weathering resistance. However, in this series white ABS exhibited a higher average tensile strength and elastic modulus, to begin with.

A clear difference between cast PA12 and PA12 manufactured with AM is seen in the ductility of the material of a non-weathered sample in Fig. 11. Although the material behaves similarly up to peak tensile strength, cast PA12 fails through consecutive iterations of visually observable necking up to over 300 mm of crosshead displacement. As a

comparison, non-weathered AM PA12 experiences a mostly brittle failure after an average of 20 mm extension and very little necking. The magnitude of tensile results is in line with [14].

The difference in mechanical performance can be attributed to numerous factors. The high amount of material porosity in AM PA12 and high surface roughness compared to injection molded samples [31] facilitate crack initiation and propagation. The polyamide semi-crystalline structure is more prone to fail from the spherulites consisting of lamellae of folded crystalline molecules [51]. The microstructure of cast PA12 is more amorphous due to faster cooling, whereas spherulite structures dominate AM PA12 microstructure especially when aged powders are used in manufacturing [18]. Diffusion of oxygen is also faster in the amorphous region facilitating oxidative degradation pathways [31] which may partly explain the more aggressive influence of accelerated weathering on the mechanical properties of cast PA12.

The porosity of parts manufactured with powder bed fusion, polymers or metals, is linked to efficient packing and melt coalescence driven by the feedstock powder size and morphology [5], and the laser energy density governed by laser energy and laser speed [5,62]. Overall porosity can be reduced with high quality feedstock powder, proper powder handling, optimal laser parameters, and post-processing steps such as hot isostatic pressing (HIP) [63] which has been found to mostly eliminate porosity. The HIP treatment will increase tensile modulus and tensile strength of the samples while reducing elongation at break.

3.4. Limitations and future perspectives

The comparison of accelerated weathering with natural weathering is not a straightforward task [22,64,65]. Environmental degradation is a complicated material-dependent process. Even though the lamps would provide a closely equivalent power distribution spectrum to sunlight, the UV irradiance in accelerated weathering is higher. Some degradation pathways have been found to behave non-linearly as a function of irradiance. Studies, where accelerated weathering have been compared to natural weathering may provide useful benchmarks [66]. For service life prediction and parameter reciprocity as a function of the UV intensity, see the work of Pickett et al. [67]. The reproducibility of results in accelerated weathering has been time and again questioned. Yet, mutual material rankings (relative degradation of materials within the

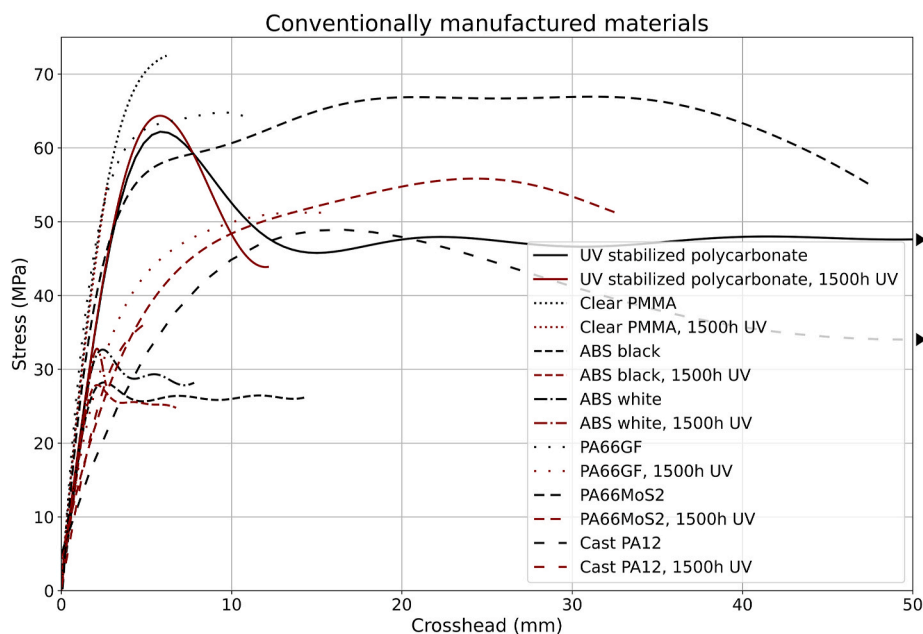


Fig. 10. A stress-crosshead displacement graph with polynomial fits of all the conventionally manufactured materials. The non-weathered materials are colored black whereas weathered samples are shown in red.

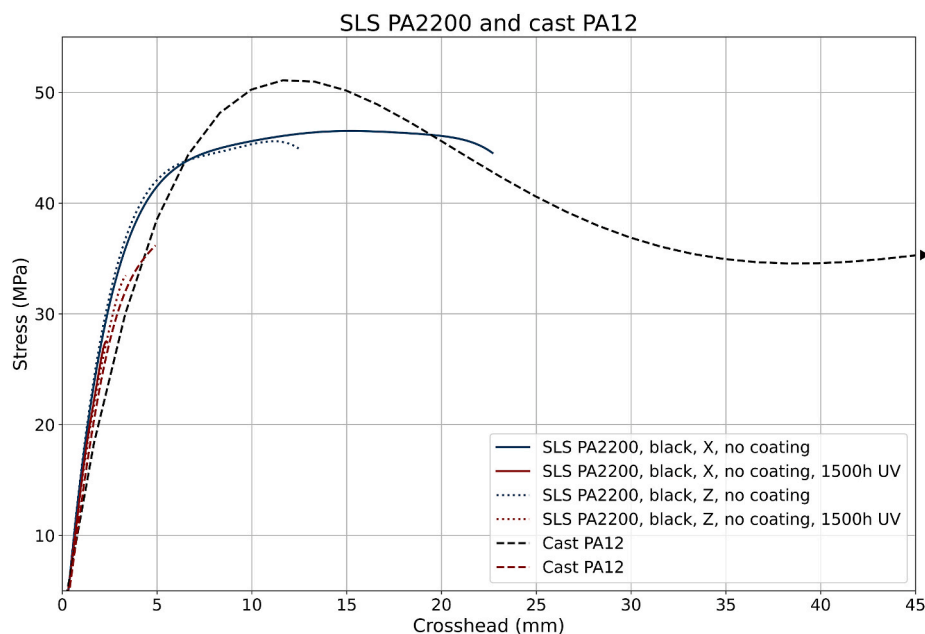


Fig. 11. Non-weathered and weathered cast PA12 compared to SLS PA12 manufactured in X and Z build orientations.

same test) have been found to correlate well irrespective of the machine or facility [19].

The degradation of plastics is a two-folded question. The environmental problems and toxicity of some polymer additives [25] is a serious concern. The accumulation of microplastic [68] in nature and the oceans threatens the whole ecosystem [69]. The engineering perspective prefers long-lasting materials that maximize resistance to weathering degradation and retain their mechanical properties. These goals are achieved via using inherently more UV stable materials, by adding chemical additives or stabilizers to the virgin polymer, compensating degradation with more material, or via protective coating and painting of surfaces. The environmental perspective, on the other hand, prefers materials that are derived from non-fossil sources, are non-toxic, do not accumulate in the environment as microplastics, and would be recyclable per the principles of the circular economy. The two goals partly collide. In general, plastics are an intriguing material category for understandable reasons. They are lightweight yet durable, easily processable even in the mass-production scale, and most of all, affordable. Many of the additives and coatings to prolong the life prediction of plastics can, unfortunately, be either toxic or inhibit material recycling after the end-of-life. A long-term solution to this problem is mostly a concern of materials research. Finding competitive alternatives to fossil-derived materials and ensuring their non-toxicity if they become an unwanted part of the ecosystem. However, design for additive manufacturing could provide a solution worth investigating to enhance the material weathering resistance of both fossil and bio-based plastics. As mentioned, degradation of parts is a surface-dependent mechanism driven mostly by the combined effect of oxygen, ionizing radiation, heat, and moisture. With a clever design for AM, a sacrificial surface texture could be made to degrade instead of the core material that provides the part with its structural integrity. Using a texturized surface instead of coating or paint would reduce the need for possible toxic components and retain a mono-material structure that is easier to recycle.

4. Conclusions

The study provides an analysis of mechanical properties and fracture characterization of non-weathered and weathered engineering plastics manufactured both with powder bed fusion AM and conventional methods. AM and cast PA12 were found to be strongly affected by the

accelerated weathering. Continuous and chopped carbon fiber reinforced polyamide with a UV varnish experienced the least changes. Weathering resistance was increased with UV coatings. However, an increase in deviation was also observed. No clear differences were found between the AM build orientations in fracture mechanisms or weathering performance. Only glass and molybdenum disulfide-filled polyamides posed clear changes in elastic modulus after weathering. All glass-filled materials increased in ductility. The behavior of molybdenum disulfide-filled samples was interestingly reversed compared to glass-filled samples with the same PA66 matrix material. This is thought to be due to changes and differences in the interfacial bonding between the polyamide matrix and reinforcement particles after weathering. Further material-specific studies are recommended combining chemical analysis, microstructure analysis, and higher resolution dynamic imaging methods to study in more detail the combined effects of environmental factors, and the AM processes on material mechanical properties and fracture mechanisms.

Data availability

The raw data required to reproduce these findings are available to download from <http://doi.org/10.5281/zenodo.5044976>. Kindly cite this article, and the dataset, if utilizing or modifying the data in your work.

CRediT authorship contribution statement

Tuomas Puttonen: Conceptualization, Data curation, Formal analysis, Investigation, Methodology, Resources, Software, Visualization, Writing – original draft, Writing – review & editing. **Mika Salmi:** Conceptualization, Project administration, Supervision, Validation, Writing – review & editing. **Jouni Partanen:** Funding acquisition, Supervision.

Declaration of competing interest

The authors declare that they have no known competing financial interests or personal relationships that could have appeared to influence the work reported in this paper.

Acknowledgements

This research was done and funded as part of a Business Finland project DIVALIITO (632/31/2018) between the Aalto University (Foundation), the Technical Research Institute of Finland (VTT), and participating consortium companies.

References

- [1] B. Gewert, M.M. Plassmann, M. Macleod, Pathways for degradation of plastic polymers floating in the marine environment, *Environ. Sci. Process. Impacts*. 17 (2015) 1513–1521, <https://doi.org/10.1039/c5em00207a>.
- [2] I. Gibson, D. Rosen, B. Stucker, *Additive Manufacturing Technologies*, second ed., Springer, 2015 <https://doi.org/10.1007/978-1-4939-2113-3>.
- [3] L.J. Tan, W. Zhu, K. Zhou, Recent progress on polymer materials for additive manufacturing, *Adv. Funct. Mater.* 30 (2020) 2003062, <https://doi.org/10.1002/ADFM.202003062>.
- [4] M. Kumke, H. Watschke, P. Hartogh, A.K. Barendiek, T. Vietor, Methods and tools for identifying and leveraging additive manufacturing design potentials, *Int. J. Interact. Des. Manuf.* 12 (2018) 481–493, <https://doi.org/10.1007/s12008-017-0399-7>.
- [5] C.A. Chatham, T.E. Long, C.B. Williams, A review of the process physics and material screening methods for polymer powder bed fusion additive manufacturing, *Prog. Polym. Sci.* 93 (2019) 68–95, <https://doi.org/10.1016/j.progpolymsci.2019.03.003>.
- [6] M. Salmi, Additive manufacturing processes in medical applications, *Materials* 14 (2021) 1–16, <https://doi.org/10.3390/ma14010191>.
- [7] C. Shuai, G. Liu, Y. Yang, F. Qi, S. Peng, W. Yang, C. He, G. Wang, G. Qian, A strawberry-like Ag-decorated barium titanate enhances piezoelectric and antibacterial activities of polymer scaffold, *Nanomater. Energy* 74 (2020) 104825, <https://doi.org/10.1016/J.NANOEN.2020.104825>.
- [8] A. Kestilä, K. Nordling, V. Miikkulainen, M. Kaipio, T. Tikka, M. Salmi, A. Auer, M. Leskelä, M. Ritala, Towards space-grade 3D-printed, ALD-coated small satellite propulsion components for fluids, *Addit. Manuf.* 22 (2018) 31–37, <https://doi.org/10.1016/J.ADDMA.2018.04.023>.
- [9] S.H. Khajavi, J. Partanen, J. Holmström, Additive manufacturing in the spare parts supply chain, *Comput. Ind. Eng.* 65 (2014) 50–63, <https://doi.org/10.1016/j.compind.2013.07.008>.
- [10] S. Chekurov, M. Salmi, Additive manufacturing in offsite repair of consumer electronics, in: *Phys. Procedia*, Elsevier B.V., 2017, pp. 23–30, <https://doi.org/10.1016/j.phpro.2017.08.009>.
- [11] S.C. Ligon, R. Liska, J. Stampfl, M. Gurr, R. Mülhaupt, Polymers for 3D printing and customized additive manufacturing, *Chem. Rev.* 117 (2017) 10212–10290, <https://doi.org/10.1021/acs.chemrev.7b00074>.
- [12] S. Chekurov, M. Salmi, V. Verboeket, T. Puttonen, T. Riipinen, A. Vaajoki, Assessing industrial barriers of additively manufactured digital spare part implementation in the machine-building industry: a cross-organizational focus group interview study, *J. Manuf. Technol. Manag.* (2021), <https://doi.org/10.1108/JMTM-06-2020-0239>.
- [13] H.J. O'Connor, A.N. Dickson, D.P. Dowling, Evaluation of the mechanical performance of polymer parts fabricated using a production scale multi jet fusion printing process, *Addit. Manuf.* 22 (2018) 381–387, <https://doi.org/10.1016/j.addma.2018.05.035>.
- [14] B. Van Hooreweder, D. Moens, R. Boonen, J.-P. Kruth, P. Sas, On the difference in material structure and fatigue properties of nylon specimens produced by injection molding and selective laser sintering, *Polym. Test.* 32 (2013) 972–981, <https://doi.org/10.1016/j.polymertesting.2013.04.014>.
- [15] S.L. Sindinger, C. Kralovec, D. Tasch, M. Schagerl, Thickness dependent anisotropy of mechanical properties and inhomogeneous porosity characteristics in laser-sintered polyamide 12 specimens, *Addit. Manuf.* 33 (2020) 101141, <https://doi.org/10.1016/j.addma.2020.101141>.
- [16] F. Calignano, F. Giuffrida, M. Galati, Effect of the build orientation on the mechanical performance of polymeric parts produced by multi jet fusion and selective laser sintering, *J. Manuf. Process.* 65 (2021) 271–282, <https://doi.org/10.1016/j.jmapro.2021.03.018>.
- [17] K. Wudy, D. Drummer, Aging effects of polyamide 12 in selective laser sintering: molecular weight distribution and thermal properties, *Addit. Manuf.* 25 (2019) 1–9, <https://doi.org/10.1016/j.addma.2018.11.007>.
- [18] S. Dadbakhsh, L. Verbelen, O. Verkinderen, D. Strobbe, P. Van Puyvelde, J. P. Kruth, Effect of PA12 powder reuse on coalescence behaviour and microstructure of SLS parts, *Eur. Polym. J.* 92 (2017) 250–262, <https://doi.org/10.1016/j.eurpolymj.2017.05.014>.
- [19] S.H. Hamid, *Handbook of Polymer Degradation*, second ed., New York, 2000, <https://doi.org/10.1201/9781482270181>.
- [20] C. Kiparissides, Polymerization reactor modeling: a review of recent developments and future directions, *Chem. Eng. Sci.* 51 (1996) 1637–1659, [https://doi.org/10.1016/0009-2509\(96\)00024-3](https://doi.org/10.1016/0009-2509(96)00024-3).
- [21] T. Lu, E. Solis-Ramos, Y. Yi, M. Kumosa, UV degradation model for polymers and polymer matrix composites, *Polym. Degrad. Stabil.* 154 (2018) 203–210, <https://doi.org/10.1016/j.polymdegradstab.2018.06.004>.
- [22] M.E. González-López, A.S. Martín del Campo, J.R. Robledo-Ortiz, M. Arellano, A. A. Pérez-Fonseca, Accelerated weathering of poly(lactic acid) and its biocomposites: a review, *Polym. Degrad. Stabil.* 179 (2020) 109290, <https://doi.org/10.1016/j.polymdegradstab.2020.109290>.
- [23] H.K. Karapanagioti, K.N. Fotopoulou, Degradation of Various Plastics in the Environment. Hazardous Chemicals Associated with Plastics in the Marine Environment, Springer, 2017, pp. 71–92. <https://doi.org/10.1007/978-1-4939-2113-3>.
- [24] B. Singh, N. Sharma, Mechanistic implications of plastic degradation, *Polym. Degrad. Stabil.* 93 (2008) 561–584, <https://doi.org/10.1016/j.polymdegradstab.2007.11.008>.
- [25] S. Karimi, E. Helal, G. Gutierrez, N. Moghimian, M. Madinehei, E. David, M. Samara, N. Demarquette, A review on graphene's light stabilizing effects for reduced photodegradation of polymers, *Crystals* 11 (2021) 3–11, <https://doi.org/10.3390/CRYST11010003>.
- [26] A.S.D. Shackelford, R.J. Williams, R. Brown, J.R. Wingham, C. Majewski, Degradation of Laser Sintered polyamide 12 parts due to accelerated exposure to ultraviolet radiation, *Addit. Manuf.* 46 (2021) 102132, <https://doi.org/10.1016/j.addma.2021.102132>.
- [27] L.D. Suits, Y.G. Hsuan, Assessing the photo-degradation of geosynthetics by outdoor exposure and laboratory weatherometer, *Geotext. Geomembranes* 21 (2003) 111–122, [https://doi.org/10.1016/S0266-1144\(02\)00068-7](https://doi.org/10.1016/S0266-1144(02)00068-7).
- [28] D. Feldman, Polymer weathering: photo-oxidation, *J. Polym. Environ.* 10 (2002) 163–173, <https://doi.org/10.1023/A:1021148205366>.
- [29] A. Roger, D. Sallet, J. Lemaire, Photochemistry of aliphatic polyamides. 3. Mechanisms of photooxidation of polyamides 6, 11, and 12 at short wavelength, *Macromolecules* 18 (1985) 1771–1775.
- [30] A. Roger, D. Sallet, J. Lemaire, Photochemistry of aliphatic polyamides. 4. Mechanisms of photooxidation of polyamides 6, 11, and 12 at long wavelengths, *Macromolecules* 19 (1986) 579–584.
- [31] A. Wörz, K. Wudy, D. Drummer, A. Wegner, G. Witt, Comparison of long-term properties of laser sintered and injection molded polyamide 12 parts, *J. Polym. Eng. Sci.* 38 (2018) 573–582, <https://doi.org/10.1515/polyeng-2017-0227>.
- [32] J.M. Pérez, J.L. Vilas, J.M. Laza, S. Arnáiz, F. Mijangos, E. Bilbao, M. Rodríguez, L. M. León, Effect of reprocessing and accelerated ageing on thermal and mechanical polycarbonate properties, *J. Mater. Process. Technol.* 210 (2010) 727–733, <https://doi.org/10.1016/j.jmatprotec.2009.12.009>.
- [33] J.M. Pérez, J.L. Vilas, J.M. Laza, S. Arnáiz, F. Mijangos, E. Bilbao, L.M. León, Effect of reprocessing and accelerated weathering on ABS properties, *J. Polym. Environ.* 18 (2010) 71–78, <https://doi.org/10.1007/s10924-009-0154-7>.
- [34] S.D. Varsavas, C. Kaynak, Weathering degradation performance of PLA and its glass fiber reinforced composite, *Mater. Today Commun.* 15 (2018) 344–353, <https://doi.org/10.1016/j.mtcomm.2017.11.008>.
- [35] J. Zhang, A. Adams, Understanding thermal aging of non-stabilized and stabilized polyamide 12 using 1H solid-state NMR, *Polym. Degrad. Stabil.* 134 (2016) 169–178, <https://doi.org/10.1016/j.polymdegradstab.2016.10.006>.
- [36] R. Seltzer, F.M. de la Escalera, J. Segurado, Effect of water conditioning on the fracture behavior of PA12 composites processed by selective laser sintering, *Mater. Sci. Eng.* 528 (2011) 6927–6933, <https://doi.org/10.1016/j.msea.2011.05.045>.
- [37] A.K. Battu, T.R. Pope, T. Varga, J.F. Christ, M.D. Fenn, W.S. Rosenthal, W. Kuang, M. Thomas, A.M. Arnold, M. Schram, M.G. Warner, C.A. Barrett, Z.C. Kennedy, Build orientation dependent microstructure in polymer laser sintering: relationship to part performance and evolution with aging, *Addit. Manuf.* 36 (2020) 101464, <https://doi.org/10.1016/j.addma.2020.101464>.
- [38] P. Chen, M. Tang, W. Zhu, L. Yang, S. Wen, C. Yan, Z. Ji, H. Nan, Y. Shi, Systematic mechanism of Polyamide-12 aging and its micro-structural evolution during laser sintering, *Polym. Test.* 67 (2018) 370–379, <https://doi.org/10.1016/j.polymertesting.2018.03.035>.
- [39] F. Yang, T. Jiang, G. Lallier, J. Bartolone, X. Chen, Process control of surface quality and part microstructure in selective laser sintering involving highly degraded polyamide 12 materials, *Polym. Test.* 93 (2021) 106920, <https://doi.org/10.1016/j.polymertesting.2020.106920>.
- [40] S. Rosso, R. Meneghello, L. Biasetto, L. Grigolato, G. Concheri, G. Savio, In-depth comparison of polyamide 12 parts manufactured by multi jet fusion and selective laser sintering, *Addit. Manuf.* 36 (2020) 101713, <https://doi.org/10.1016/j.addma.2020.101713>.
- [41] L. Lanzl, K. Wudy, D. Drummer, The effect of short glass fibers on the process behavior of polyamide 12 during selective laser beam melting, *Polym. Test.* 83 (2020) 106313, <https://doi.org/10.1016/j.polymertesting.2019.106313>.
- [42] H.J. O'Connor, D.P. Dowling, Comparison between the properties of polyamide 12 and glass bead filled polyamide 12 using the multi jet fusion printing process, *Addit. Manuf.* 31 (2020) 100961, <https://doi.org/10.1016/j.addma.2019.100961>.
- [43] Y. Liu, L. Zhu, L. Zhou, Y. Li, Microstructure and mechanical properties of reinforced polyamide 12 composites prepared by laser additive manufacturing, *Rapid Prototyp. J.* 25 (2019) 1127–1134, <https://doi.org/10.1108/RPJ-08-2018-0220>.
- [44] M.R. Khosravani, F. Berto, M.R. Ayatollahi, T. Reinicke, Fracture behavior of additively manufactured components: a review, *Theor. Appl. Fract. Mech.* 109 (2020) 102763, <https://doi.org/10.1016/j.tafmec.2020.102763>.
- [45] T. Puttonen, M. Salmi, J. Partanen, Mechanical Properties and Fracture Characterization of Additive Manufacturing Polyamide 12 after Accelerated Weathering, *Zenodo*, 2021. <http://doi.org/10.5281/zenodo.5044976>.
- [46] S. Preibisch, S. Saalfeld, P. Tomancak, Globally optimal stitching of tiled 3D microscopic image acquisitions, *Bioinformatics* 25 (2009) 1463–1465, <https://doi.org/10.1093/bioinformatics/btp184>.
- [47] B. Fayolle, X. Colin, L. Audouin, J. Verdu, Mechanism of degradation induced embrittlement in polyethylene, *Polym. Degrad. Stabil.* 92 (2007) 231–238, <https://doi.org/10.1016/J.POLYMDEGRADSTAB.2006.11.012>.

- [48] K.N. Cundiff, Y. Madi, A.A. Benzerga, Photo-oxidation of semicrystalline polymers: damage nucleation versus growth, *Polymer* 188 (2020) 122090, <https://doi.org/10.1016/J.POLYMER.2019.122090>.
- [49] O. Okamba-Diogo, E. Richaud, J. Verdu, F. Fernagut, J. Guilment, B. Fayolle, Investigation of polyamide 11 embrittlement during oxidative degradation, *Polymer* 82 (2016) 49–56, <https://doi.org/10.1016/J.POLYMER.2015.11.025>.
- [50] A. Du Plessis, I. Yadroitsev, I. Yadroitsava, S.G. Le Roux, X-ray microcomputed tomography in additive manufacturing: a review of the current technology and applications, *3D Print. Addit. Manuf.* 5 (2018) 227–247, <https://doi.org/10.1089/3dp.2018.0060>.
- [51] L. Safai, J.S. Cuellar, G. Smit, A.A. Zadpoor, A review of the fatigue behavior of 3D printed polymers, *Addit. Manuf.* 28 (2019) 87–97, <https://doi.org/10.1016/j.addma.2019.03.023>.
- [52] P.D. Evans, J.G. Haase, A.S.B.M. Seman, M. Kiguchi, The search for durable exterior clear coatings for wood, *Coatings* 5 (2015) 830–864, <https://doi.org/10.3390/COATINGS5040830>.
- [53] S.K. Dhoke, A.S. Khanna, Electrochemical behavior of nano-iron oxide modified alkyd based waterborne coatings, *Mater. Chem. Phys.* 117 (2009) 550–556, <https://doi.org/10.1016/J.MATCHEMPHYS.2009.07.010>.
- [54] L. Jiang, M. Zhou, Y. Ding, Y. Zhou, Y. Dan, Aging induced ductile-brittle-ductile transition in bisphenol A polycarbonate, *J. Polym. Res.* 25 (2018) 1–9, <https://doi.org/10.1007/s10965-018-1443-4>.
- [55] V. Titone, M.C. Mistretta, L. Botta, F.P. La Mantia, Investigation on the properties and on the photo-oxidation behaviour of polypropylene/fumed silica nanocomposites, *Polymers* 13 (16) (2021) 2673, <https://doi.org/10.3390/POLYM13162673>.
- [56] J.F. Larché, P.O. Bussière, S. Thérias, J.L. Gardette, Photooxidation of polymers: relating material properties to chemical changes, *Polym. Degrad. Stabil.* 97 (2012) 25–34, <https://doi.org/10.1016/J.POLYMDEGRADSTAB.2011.10.020>.
- [57] X.F. Wei, K.J. Kallio, S. Bruder, M. Bellander, H.H. Kausch, U.W. Gedde, M. S. Hedenqvist, Diffusion-limited oxidation of polyamide: three stages of fracture behavior, *Polym. Degrad. Stabil.* 154 (2018) 73–83, <https://doi.org/10.1016/j.polymdegradstab.2018.05.024>.
- [58] Ö. Özgenç, S. Durmaz, S. Şahin, İ.H. Boyacı, Evaluation of the weathering resistance of waterborne acrylic- and alkyd-based coatings containing HALS, UV absorber, and bark extracts on wood surfaces, *J. Coating Technol. Res.* 17 (2019) 461–475, <https://doi.org/10.1007/S11998-019-00293-4>, 2020.
- [59] N.S. Allen, R. McIntyre, J.M. Kerrod, C. Hill, M. Edge, Photo-stabilisation and UV blocking efficacy of coated macro and nano-rutile titanium dioxide particles in paints and coatings, *J. Polym. Environ.* 26 (2018) 4243–4257, <https://doi.org/10.1007/S10924-018-1298-0>.
- [60] L.N. Chang, W.S. Chow, Accelerated weathering on glass fiber/epoxy/organo-montmorillonite nanocomposites, *J. Compos. Mater.* 44 (2010) 1421–1434, <https://doi.org/10.1177/0021998309360944>.
- [61] J.R. Wingham, M. Omran, J. Shepherd, C. Majewski, Effect of steam autoclaving on laser sintered polyamide 12, *Rapid Prototyp. J.* (2020), <https://doi.org/10.1108/RPJ-11-2019-0288>.
- [62] Y. Yang, C. Lu, S. Peng, L. Shen, D. Wang, F. Qi, C. Shuai, Laser Additive Manufacturing of Mg-Based Composite with Improved Degradation Behaviour, 2020, pp. 278–293, <https://doi.org/10.1080/17452759.2020.1748381>. 15.
- [63] C.S. Abbott, M. Sperry, N.B. Crane, Relationships between porosity and mechanical properties of polyamide 12 parts produced using the laser sintering and multi-jet fusion powder bed fusion processes, *J. Manuf. Process.* 70 (2021) 55–66, <https://doi.org/10.1016/J.JMAPRO.2021.08.012>.
- [64] J.E. Pickett, O. Kuvshinnikova, L.P. Sung, B.D. Ermi, Accelerated weathering parameters for some aromatic engineering thermoplastics. Part 2: polycarbonate copolymers, polyarylate and ABS, *Polym. Degrad. Stabil.* 181 (2020) 109330, <https://doi.org/10.1016/j.polymdegradstab.2020.109330>.
- [65] J.E. Pickett, O. Kuvshinnikova, L.-P. Sung, B.D. Ermi, Accelerated weathering parameters for some aromatic engineering thermoplastics, *Polym. Degrad. Stabil.* 166 (2019) 135–144, <https://doi.org/10.1016/J.POLYMDEGRADSTAB.2019.05.028>.
- [66] R.M. Santos, G.L. Botelho, A.V. Machado, Artificial and natural weathering of ABS, *J. Appl. Polym. Sci.* 116 (4) (2010) 2005–2014, <https://doi.org/10.1002/app.31663>.
- [67] J.E. Pickett, Weathering of plastics, in: *Handb. Environ. Degrad. Mater.*, third ed., Elsevier Inc., 2018, pp. 163–184, <https://doi.org/10.1016/B978-0-323-52472-8.00008-3>.
- [68] A.L. Andrady, The plastic in microplastics: a review, *Mar. Pollut. Bull.* 119 (2017) 12–22, <https://doi.org/10.1016/j.marpolbul.2017.01.082>.
- [69] A. Chamas, H. Moon, J. Zheng, Y. Qiu, T. Tabassum, J. Hee Jang, M. Abu-Omar, S. L. Scott, S. Suh, Degradation rates of plastics in the environment, *ACS Sustain. Chem. Eng.* 8 (9) (2020) 3494–3511, <https://doi.org/10.1021/acssuschemeng.9b06635>.